ACS APPLIED MATERIALS & INTERFACES

RESEARCH ARTICLE

www.acsami.org

High Photocatalytic Activity of ZnO−Carbon Nanofiber Heteroarchitectures

Jingbo Mu,[†] Changlu Shao,[*,‡] Zengcai Guo,[†] Zhenyi Zhang,[‡] Mingyi Zhang,[‡] Peng Zhang,[‡] Bin Chen,[*,†] and Yichun Liu[‡]

[†]Department of Chemistry, Northeast Normal University, 5268 Renmin Street, Changchun 130024, People's Republic of China

[‡]Center for Advanced Optoelectronic Functional Materials Research and Key Laboratory of UV Light-Emitting Materials and Technology of Ministry of Education, Northeast Normal University, 5268 Renmin Street, Changchun 130024, People's Republic of China

ABSTRACT: One-dimensional ZnO−carbon nanofibers (CNFs) heteroarchitectures with high photocatalytic activity have been successfully obtained by a simple combination of electrospinning technique and hydrothermal process. The as-obtained products were characterized by field-emission scanning electron microscopy (FE-SEM), energy-dispersive X-ray (EDX) spectroscopy, transmission electron microscopy (TEM), X-ray diffraction (XRD), X-ray photoelectron spectroscopy (XPS), and IR spectrum. The results revealed that the secondary ZnO nanostructures were successfully grown on the primary CNFs substrates without aggregation. And, the coverage density of ZnO nanoparticles coating on the surface of the CNFs could be controlled by simply adjusting the mass ratio of zinc acetate to CNFs in the precursor during the hydrothermal process for the fabrication of ZnO−CNFs heterostructures. The obtained ZnO−CNFs heteroarchitectures showed high photocatalytic property to degrade rhodamine B (RB) because of the formation of heteroarchitectures, which might improve the separation of photogenerated electrons and holes. Moreover, the ZnO−CNFs heteroarchitectures could be easily recycled without the decrease in photocatalytic activity due to their one-dimensional nanostructural property.

KEYWORDS: ZnO, CNFs, heteroarchitectures, photocatalysis, degradation

1. INTRODUCTION

Environmental problems such as organic pollutants and toxic water pollutants produced by some industries are harmful to human health and the general well-being of man. Photocatalysis, as a "green" technique, offers great potential for complete elimination of toxic chemicals in the environment through its efficiency and broad applicability.[1] It has been reported that the nanostructural semiconductor metal oxides can degrade various organic pollutants under UV light irradiation. Thus, in recent years, many kinds of semiconductor metal oxide nanophotocatalyst, such as Bi_2O_3, Fe_2O_3, TiO_2, ZnO, and so forth, have been developed for creating a comfortable environment for human beings.[2−5] Among these semiconductor metal oxide photocatalysis, TiO_2 and ZnO have been recognized as the excellent materials for photocatalytic process because of their high photosensitivity, nontoxic nature, and large band gap.[6−9] Although TiO_2 is extensively investigated and widely employed, ZnO is also a suitable alternative to TiO_2 due to their similar bandgap energy (3.2 eV) and its lower cost. Moreover, some studies have highlighted that ZnO exhibits a better efficiency than TiO_2 in photocatalytic degradation of some dyes in aqueous solution.[10−13] However, enhancing the photocatalytic efficiency of ZnO to meet the practical application requirements is still a challenge because of the bottleneck of poor quantum yield caused by the rapid recombination of photogenerated electrons and holes.[14,15] Thus, several attempts have been made to reduce the recombination of photoinduced electron−hole pairs during the photocatalytic reactions by conjugation of the photocatalysts with electron scavenging agents such as metals, metal oxides or organic molecules.[16−19]

Recently, one-dimensional carbon nanofibers (CNFs) have been widely used as ideal electron pathways due to their good conductivity ($\rho = (3-7) \times 10^{-3}\ \Omega$ cm).[20,21] Some results have demonstrated that CNFs could efficiently capture and transport of photogenerated electrons through highly conductive long CNFs.[21,22] Judging from the excellent photocatalyst of ZnO and the efficient electron transfer property of CNFs, combination of ZnO and CNFs seems to be ideal for hindering the recombination of electrons and holes and improving the photocatalytic efficiency.

To date, there has been no report on the fabrication of ZnO−CNFs heteroarchitectures photocatalyst with efficient electron−hole separation ability. Herein, we reported a successful attempt for the fabrication ZnO−CNFs heterostructures via simple electrospinning technique and hydrothermal method, and the photocatalytic activity of these heterostructures photocatalysts were investigated by measuring the degradation of dye RB as a test substance. The experimental results showed that the as-obtained ZnO−CNFs heterostructures exhibited excellent photocatalytic activity. Moreover, due to the large length to diameter ratio of CNFs, the ZnO−CNFs heterostructures could be reclaimed easily by sedimentation without a decrease of the photocatalytic activity. Finally, the mechanisms of photocatalysis enhancement in ZnO−CNFs heterostructures were proposed.

Received: November 28, 2010
Accepted: January 18, 2011
Published: February 3, 2011

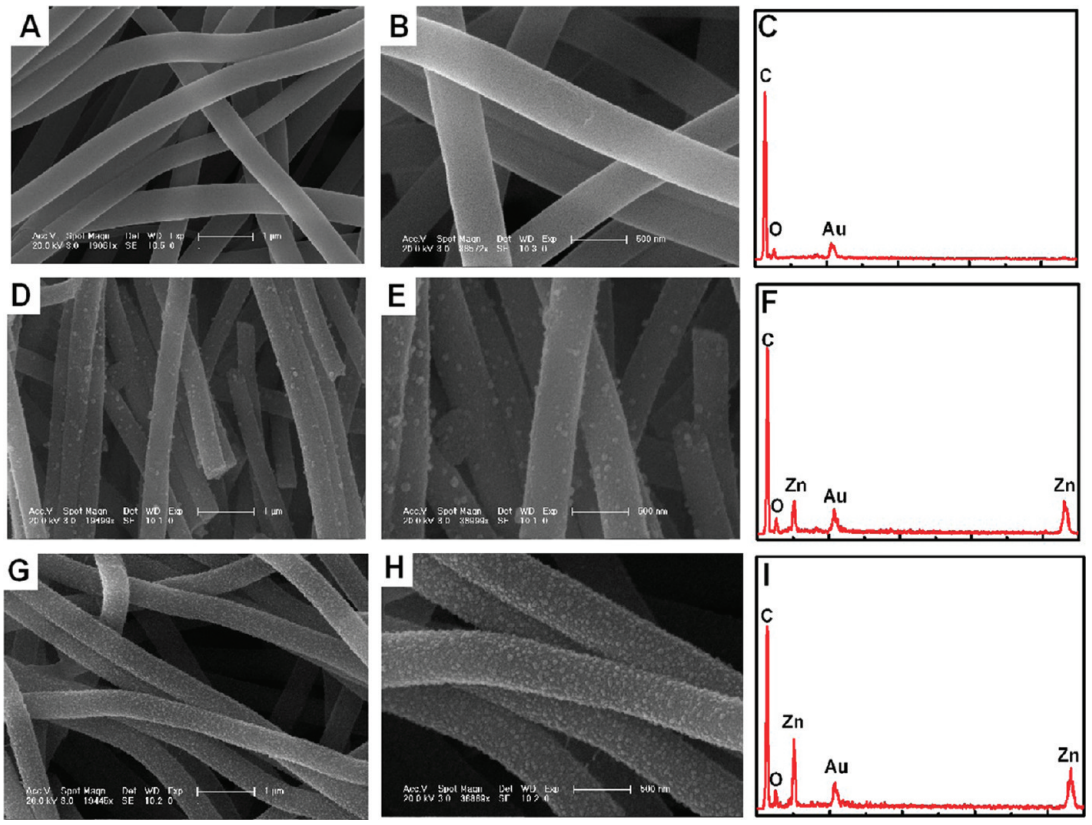

Figure 1. (A) Low-magnification SEM image of the pure CNFs. (B) High-magnification SEM image of the pure CNFs. (C) EDX spectrum of the pure CNFs. (D) Low-magnification SEM image of the sample ZC1. (E) High-magnification SEM image of the sample ZC1. (F) EDX spectrum of sample ZC1. (G) Low-magnification SEM image of the sample ZC2. (H) High-magnification SEM image of the sample ZC2. (I) EDX spectrum of sample ZC2.

2. MATERIALS AND METHODS

2.1. Preparation of the Carbon Nanofibers. In our experiments, the preparing process consisted of two steps. First, 1.5 g of polyacrylonitrile (PAN) (Mw = 150 000) powders were dissolved in 10 mL of *N*,*N*-dimethylformamide (DMF) solution. After stirring at room temperature for 12 h, the above precursor solutions were drawn into a hypodermic syringe for electrospinning. The positive voltage applied to the tip was 10 kV and the distance between the needle tip and the collector was 10 cm. The as-spun PAN fibers were collected on aluminum foil that was attached on the edge of the collecting wheel. For carbonization, the substrates were placed in a tube furnace and stabilized in air for 60 min at 270 °C, then carbonized in nitrogen at 1000 °C at a ramp rate was 5 °C/min, and finally cooled to room temperature. Thus, carbon electrospun nanofibers (CNFs) were obtained.

2.2. Fabrication of ZnO−CNFs Heterostructures. First, zinc acetate and the obtained CNFs (with the mass ratio of 4:1) were put into 15 mL of deionized water. Then, 0.5 mol/L NaOH solution was dropped into the solution until the pH reached 10 under continuous magnetic stirring. The obtained mixture was transferred into a 20 mL Teflon-lined stainless autoclave, sealed and maintained at 180 °C for 12 h, and then cooled to room temperature. The as-fabricated products were collected, washed several times with ethanol and deionized water, respectively, and then dried at 70 °C for 12 h. Thus, the ZnO−CNFs heterostructures were fabricated, which was denoted as ZC1. By this method, the sample prepared at the mass ratio of zinc acetate to CNFs at 8:1 was denoted as ZC2. In addition, for contrast, the ZnO was obtained in the absence of CNFs during the process of prepartion of the ZnO−CNFs heterostructures and ready for further test.

2.3. Characterization. The scanning electron microscopy (SEM, XL-30 ESEM FEG, Micro FEI Philips) and transmission electron microscopy (TEM; high resolution TEM [HRTEM], JEM-3010) were used to characterize the morphologies of the products. Energy dispersive X-ray (EDX) spectroscopy being attached to scanning electron microscopy (SEM) was used to analyze the composition of samples. X-ray diffraction (XRD) measurement was carried out using a D/max 2500 XRD spectrometer (Rigaku) with Cu Ka line of 0.1541 nm. X-ray photoelectron spectroscopy (XPS) was performed on a VG ESCALAB LKII instrument with Mg KR-ADES ($h\nu$ = 1253.6 eV) source at a residual gas pressure of below 1×10^{-8} Pa. Fourier transform infrared (FT-IR) spectra were obtained on Magna 560 FT-IR spectrometer with a resolution of 1 cm^{-1}. The photoluminescence (PL) spectra of photocatalysts were detected with a Jobin Yvon HR800 micro-Raman spectrometer using a 325 nm line from a He−Cd laser.

2.4. Photocatalytic Test. The photoreactor was designed with an internal light source surrounded by a quartz jacket (50 W high-pressure mercury lamp with main emission wavelength of 313 nm), where the suspension includes the nanofiber catalyst and an aqueous RB (100 mL, 10 mg/L) completely surrounding the light source. The solution was stirred in the dark for 30 min to obtain a good dispersion and establish adsorption−desorption equilibrium between the organic molecules and the catalyst surface. Decreases in the concentrations of dyes were analyzed by a Cary 500 UV−vis−NIR spectrophotometer. At given intervals of illumination, the samples of the reaction solution were taken out and analyzed.

3. RESULTS AND DISCUSSIONS

Figure 1 showed the morphology characterization of the pure CNFs and the as-obtained samples. Images A and B in Figure 1 showed the typical SEM images of the electrospun carbon nanofibers. From Figure 1A, it could be observed that the pure

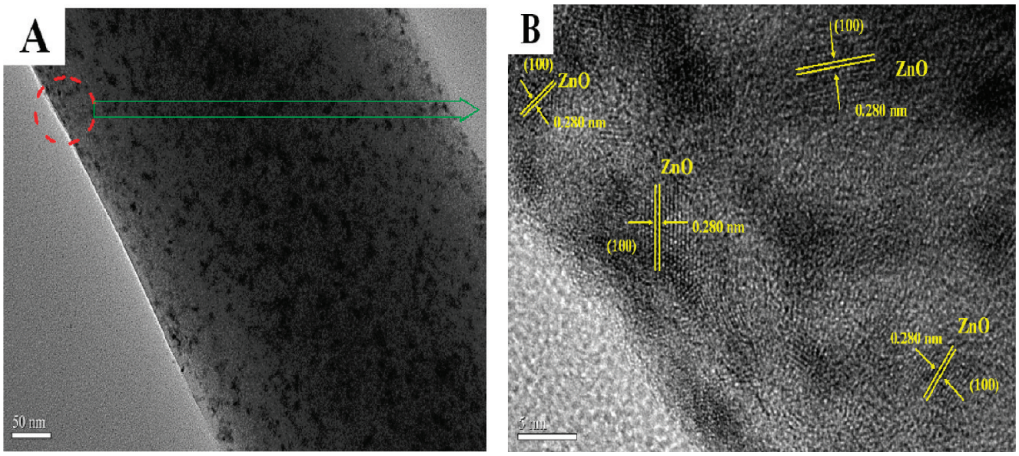

Figure 2. (A) TEM image of the sample ZC2. (B) HRTEM image of the sample ZC2.

CNFs aligned in random orientation because of the bending instability associated with the spinning jet. Figure 1B displayed the corresponding SEM image with higher magnification. It was showed that these randomly oriented CNFs had a smooth and uniform surface without secondary nanostructures, and the diameter of the CNFs ranged from 400 to 450 nm. SEM image of the sample ZC1 shown in Figure 1D indicated that there was essentially no change to the nanofibers' morphology during the growth of the ZnO nanoparticles. Figure 1E was the higher-magnification image of the sample ZC1, it could be observed that the nanoparticles were uniformly distributed across the surface of each fiber without aggregation, offering the high level exposure of the nanoparticles' surface. Images G and H in Figure 1 revealed the different magnified image of sample ZC2. It could be observed that the density of the nanoparticles was dramatically increased when the precursor molar ratio of reactants was increased. It was worth pointing out that the surface area of CNFs was advantageous for uniform growth and distribution of ZnO nanoparticles on the surface of CNFs. Figure 1C, F, and I were the energy-dispersive X-ray (EDX) spectrum of the samples CNFs, ZC1, and ZC2, respectively. It was indicated that C and O elements existed in pure electropun CNFs, whereas C, O, and Zn existed in the ZnO−CNFs heterostructures (ZC1 and ZC2), respectively. The EDX spectrum further confirmed that the ZnO−CNFs heteroarchitectures were successfully fabricated.

To obtain the microstructure of the ZnO−CNFs heteroarchitectures, the TEM images depicted in Figure 2 provided a clear observation of the as-synthesized ZC2 sample. The low-magnification TEM image of the ZnO−CNFs heteroarchitectures was displayed in Figure 2A. It could be seen that the ultrasonic process during the sample preparation for TEM measurements did not caused the ZnO nanoparticles to fall off the CNFs, it indicated that ZnO nanoparticles had been successfully grown onto the surface of the CNFs. Moreover, it could be observed that the diameter of CNFs was about 400 nm, which was in agreement with the SEM analysis above. Meanwhile, a high-resolution image of the ZC2 sample obtained from the area marked with a red circularity in Figure 2A was shown in Figure 2B, which revealed that ZnO nanoparticles were uniformly attached on the surface of the CNFs. The image revealed the simultaneous presence of the crystalline ZnO and carbon. As observed in Figure 2B, the interplanar distances of 0.280 nm agreed well with the lattice spacing of the (100) planes of the hexagonal wurtzite ZnO. And the interplanar spacings were usually different from each other for CNFs, which indicated the low crystallinity of the carbon. These results confirmed that the heteroarchitectures were well-formed between ZnO nanoparticles and CNFs.

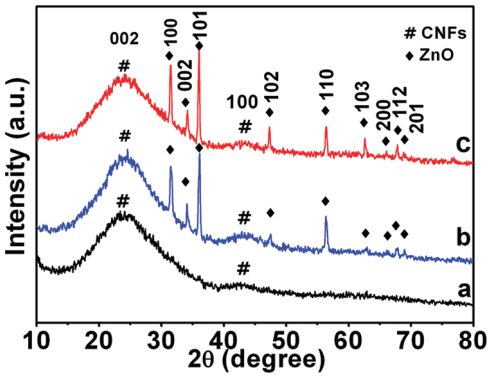

Figure 3. XRD patterns of the samples (a) CNFs, (b) ZC1, and (c) ZC2.

The X-ray diffraction (XRD) patterns of the as-obtained samples and pure CNFs were shown in Figure 3. From Figure 3a−c, the broad peaks centered at around 25 and 44° were attributed to the (002) and (100) planes of the carbon structure in CNFs. And, compared with the pure CNFs, the diffraction peaks of ZnO were also clearly observed in Figure 3a and b, which could be perfectly indexed as the hexagonal wurtzite structure for ZnO (JCPDS 36−1451). No characteristic peaks for impurity, such as Zn, ZnO_2 and $ZnCO_3$ were observed, suggesting that the composition of the above nanofibers was ZnO and CNFs. Moreover, the average grain sizes of the products were calculated by applying the Debye−Scherrer formula, $D = K\lambda/(\beta \cos \theta)$, where λ was the wavelength of the X-ray radiation (Cu Kα = 0.15406 nm), K was a constant taken as 0.89, β was the line width at half-maximum height, and θ was the diffracting angle. The average particle size had been calculated using the three different prominent planes of (100), (101), and (110) with mean values of 18.23 and 12.45 nm for ZC1 and ZC2, respectively. It is worthwhile to note that the diffraction peaks of ZnO in ZC1 as well as in ZC2 were sharp and intense, implying the high crystallinity of the ZnO nanoparticles in the ZnO−CNFs heteroarchitectures.

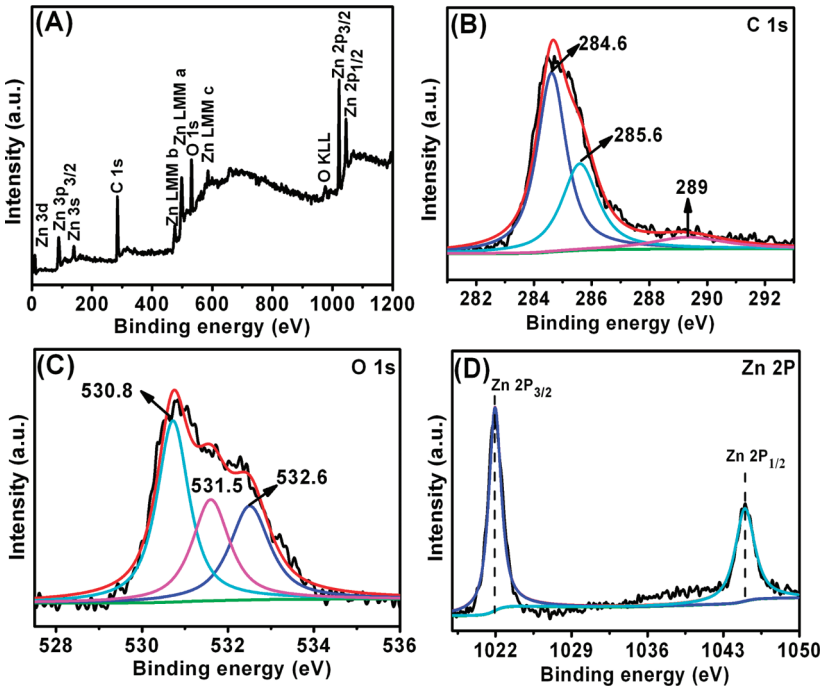

Figure 4. (A) XPS fully scanned spectra of the sample ZC2; (B) C 1s scan; (C) O 1s scan; (D) Zn 2p scan.

To confirm the chemical composition of the prepared heterostructures, the sample ZC2 was further studied by XPS analysis. A wide survey scan of XPS spectra was taken in the range 0−1200 eV as shown in Figure 4A. No extra peak corresponding to any impurities other than C, Zn and O were observed in the figure. The high resolution XPS spectrum for the C 1s region around 285 eV was shown in Figure 4B. The binding energy with peak at 284.6 eV was attributed to extensively delocalized alternant hydrocarbon,[23] the peak at 285.6 eV was characteristic of the combination of C−C bands.[24] Moreover, the peak of carboxyl carbon (O−C═O) was located at 289 eV.[25] The O 1s XPS spectrum could be resolved using the XPS peak fitting program, version 4.1. In Figure 4C, it was showed that each O 1s XPS peak was wide and asymmetric, demonstrating that there were more than one chemical state. The lower binding energy component at 530.8 eV was attributed to the wurtzite structure of hexagonal Zn^{2+} ion of the metal oxide.[26] And the other peaks at 531.5 and 532.6 eV were related to surface hydroxyl groups (O−H), oxygen making single bonds carbon (C−O),[27] respectively. The Zn 2p spectrum in Figure 4D showed two symmetric peaks, the peak centered at 1021.9 eV corresponded to the Zn $2p_{3/2}$ and another one centered at 1044.9 eV was assigned to Zn $2p_{1/2}$, indicating a normal state of Zn^{2+} in the ZnO−CNFs heterostructures. These results further confirmed that the heterostructures were composed of ZnO and CNFs. Moreover, by XPS analysis, the mass ratios of CNFs to ZnO were determined to be 3:5 and 3:8 for ZC1 and ZC2, respectively.

Figure 5 showed the FT-IR spectral analysis of the pure CNFs, ZC1 and ZC2 samples. In Figure 4a−c, it was observed that the CNFs exhibited strong peaks. The broad band at 1200 cm^{-1} was attributed to the C−C stretching vibration.[28−30] The peak at 1540 cm^{-1} corresponded to the asymmetric and symmetric stretching band of COO^-. The peaks at around 2930 cm^{-1} and 2860 cm^{-1} were assigned to the stretching vibration of the methylene ($-CH_2-$) group. The peak at 3420 cm^{-1} corresponded to the −OH stretching mode. Notably, by comparing

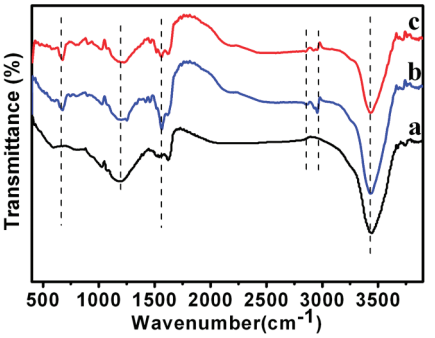

Figure 5. FT-IR spectra of samples (a) CNFs, (b) ZC1, and (c) ZC2.

the FT-IR spectrum of the pure CNFs (Figure 4c), the characteristic peaks, observed at about 623 cm^{-1}[31,32] in Figure 4a and b, were typical for the Zn−O−Zn antisymmetric and symmetric vibrations for the ZnO−CNFs heteroarchitectures. These FT-IR spectra provided the useful information that the ZnO were successfully attached to the CNFs.

To demonstrate the photoactivity of the as-obtained ZnO−CNFs heteroarchitectures for the degradation of organic pollutants, we carried out the experiments of the photocatalytic degradation of rhodamine B (RB) as a test reaction. Furthermore, in the comparative experiments, the pure ZnO was used as a photocatalytic reference to understand the photocatalytic activity of the ZnO−CNFs heteroarchitectures. The change in absorption spectra of RhB aqueous solution showed the change of its concentration. The initial concentration (C_0), the final concentration (C), and the degradation rate (D%) had a mathematical expression as follows

$$D\% = \frac{C_0 - C}{C_0} 100\% \quad (1)$$

dx.doi.org/10.1021/am101171a |ACS Appl. Mater. Interfaces 2011, 3, 590–596

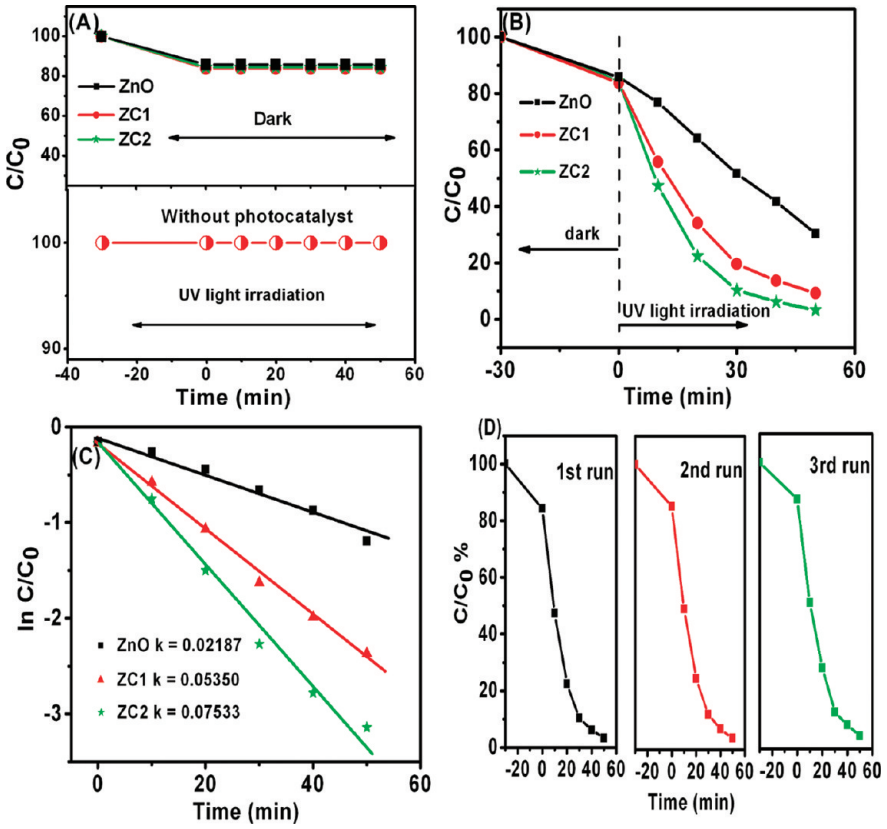

Figure 6. (A) Degradation profiles of RB in the presence of the photocatalysts but in the dark and with UV light irradiation but in the absence of the photocatalysts. (B) Degradation profiles of RB over the samples: ZC1, ZC2, and ZnO. (C_0 = 10 mg/L, catalyst 0.1 g). (C) Kinetic linear simulation curves of RB photocatalytic degradation with two samples: ZC1, ZC2, and ZnO. (D) Photocatalytic activity of the ZnO−CNFs heteroarchitectures (ZC2) for RB degradation with three times of cycling uses.

As observed in Figure 6A, the control experiments were performed under different conditions: (1) in the presence of photocatalysts but in the dark and (2) with UV irradiation but in the absence of the photocatalysts. These control experiments revealed that there was no appreciable degradation of RB over the ZnO−CNFs heteroarchitectures in the absence of UV light irradiation, indicating that the adsorption of RB on the ZnO−CNFs heteroarchitectures could be negligible. And, there was no appreciable degradation of RB after 50 min in the absence of photocatalysts. However, as observed in Figure 6B, after UV light irradiation for 50 min, the degradation efficiency of RB were about 70, 90, and 96% for the ZnO, ZC1, and ZC2. Obviously, the ZnO−CNFs heteroarchitectures showed much higher photocatalytic activities than that of ZnO. So RB could be degraded efficiently when UV light was used as the light source in the presence of the ZnO−CNFs heteroarchitectures photocatalyst. The kinetic linear simulation curves of the photocatalytic degradation of RB over the above catalysts showed that the above degradation reactions followed a Langmuir−Hinshelwood apparent first-order kinetics model due to the low initial concentrations of the reactants. The explanation was described below[33]

$$r = dC/dt = kKC/(1 + KC) \quad (2)$$

where r was the degradation rate of the reactant (mg/(L min)), C was the concentration of the reactant (mg/L), t was the UV light irradiation time, k was the reaction rate constant (mg/(Lmin)), and K was the adsorption coefficient of the reactant (L/mg). When the initial concentration (C_0) was very low (C_0 = 10 mg/L for RB in the present experiment), eq 2 could be simplified to an apparent first-order model[34]

$$\ln C_0/C = kKt = k_{app}t \quad (3)$$

where k_{app} was the apparent first-order rate constant (min^{-1}). The determined k_{app} for different catalysts were summarized in Figure 6C. The photocatalytic reactivity order was ZC2 > ZC1> ZnO. Moreover, the stability of the ZnO−CNFs heteroarchitectures (ZC2) was examined for degradation of RB during a three cycle experiment, which was very important for the ZnO−CNFs heteroarchitectures to apply in environmental technology. As shown in Figure 6D, the photocatalytic degradation of RB over the ZnO−CNFs heteroarchitectures under UV light irradiation was effective. More importantly, it was indicated that these heteroarchitectures nanofibers photocatalysts with high photocatalytic activity could be easily separated and recovered by sedimentation, and would greatly promote their practical application to eliminate the organic pollutants from wastewater.

On the basis of the above results, a proposed mechanism was being discussed to explain the enhancement of the photocatalytic properties of the ZnO−CNFs heteroarchitectures. It was shown in Figure 7a. The mechanism was that the CNFs supported catalysts were believed to exhibit cooperative or synergetic effects between CNFs and semiconductive metal oxides. Here, a high-energy photon excites an electron from the valence band to the conduction band of ZnO, photogenerated electrons in ZnO may move freely toward the surface of the CNFs and excess of valence

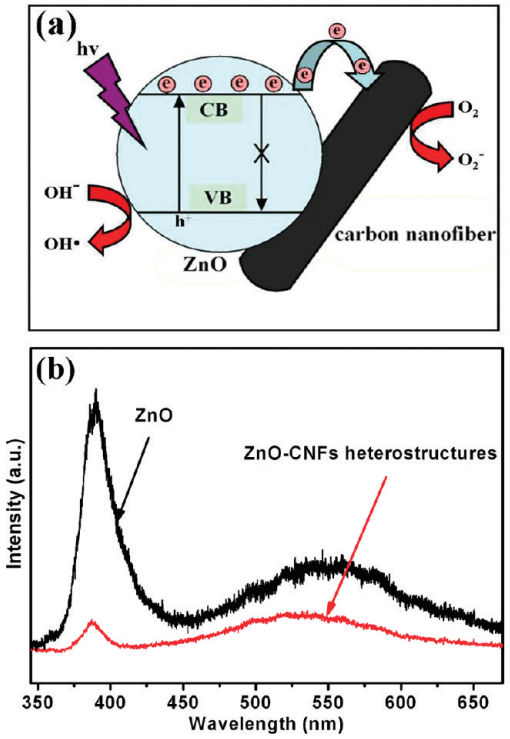

Figure 7. (a) Proposed mechanisms for the photocatalysis of the ZnO−CNFs heteroarchitectures. The CNF serves as an electron sink, and scavenges away the electrons hindering recombination. (b) PL emission spectra of ZnO and ZnO−CNFs heterostructures.

band holes were left in the ZnO to migrate to the surface and react with H_2O or OH^- to produce active species such as OH•,[35] suggesting that the photogenerated electrons and holes were efficiently separated. Furthermore, the better separation of photogenerated electrons and holes in the ZnO−CNFs heterostructures was confirmed by PL emission spectra of ZnO and ZC2. In Figure 7b, it was indicated that the ZnO−CNFs heteroarchitectures exhibited much lower emission intensity than ZnO, indicating that the recombination of the photogenerated charge carrier was inhibited greatly in the ZnO−CNFs heterostructures. The efficient charge separation could increase the lifetime of the charge carriers and enhance the efficiency of the interfacial charge transfer to adsorbed substrates, and then account for the higher activity of the ZnO−CNFs heteroarchitectures photocatalyst. The mechanism for the photocatalytic degradation of RB in our experiment was proposed as follows

$$(\mathrm{ZnO}-\mathrm{CNFs}) + h\nu \rightarrow e^-(\mathrm{CNFs}) + h^+(\mathrm{ZnO})$$

$$e^- + \mathrm{O_2} \rightarrow \mathrm{O_2}\cdot^-$$

$$h^+ + \mathrm{OH}^- \rightarrow \mathrm{OH}\cdot$$

$$\mathrm{O_2}\cdot^- + \mathrm{H_2O} \rightarrow \mathrm{HO_2}\cdot + \mathrm{OH}^-$$

$$\mathrm{HO_2}\cdot + \mathrm{H_2O} \rightarrow \mathrm{H_2O_2} + \mathrm{OH}\cdot$$

$$\mathrm{H_2O_2} \rightarrow 2\mathrm{OH}\cdot$$

$$\mathrm{OH}\cdot + \mathrm{RB} \rightarrow \mathrm{CO_2} + \mathrm{H_2O}$$

Under UV light irradiation, photogenerated electrons in ZnO moved freely to the surface of the CNFs, meanwhile, the photogenerated holes were left in the valence band of ZnO. Subsequent to various steps, the holes (h^+) were ultimately trapped by surface hydroxyl groups (or H_2O) at the catalyst surface to yield OH• radicals. Dissolved oxygen molecules react with the surface of the CNFs electrons (e^-) to yield superoxide radical anions, $O_2\bullet^-$, which on protonation generate the hydroperoxy, $HO_2\bullet$, radicals, producing hydroxyl radical OH•, which was a strong oxidizing agent to decompose the organic dye.[36,37]

CONCLUSION

In summary, the ZnO−CNFs heteroarchitectures fabricated via the electrospinning and hydrothermal methods possessed higher photocatalytic activities than the pure ZnO for the degradation of RB dye under UV light irradiation. Furthermore, the ZnO−CNFs heteroarchitectures nanofibers could be easily recycled without decrease of the photocatalytic activity due to their one-dimensional nanostructure property. And it is expected that the ZnO−CNFs heterostructured nanofibers with high photocatalytic activity will greatly promote their practical application to eliminate the organic pollutants from wastewater.

AUTHOR INFORMATION

Corresponding Author

*E-mail: clshao@nenu.edu.cn (C.S.); chenb608@nenu.edu.cn (B.C.). Tel. 8643185098803.

ACKNOWLEDGMENT

The present work is supported financially by the National Natural Science Foundation of China (50572014, 50972027, and 10647108) and the Program for New Century Excellent Talents in University (NCET-05-0322).

REFERENCES

(1) Hoffmann, M. R.; Martin, S. T.; Choi, W.; Bahnemannt, D. W. *Chem. Rev.* **1995**, *95*, 69–96.
(2) Wang, C.; Shao, C.; Liu, Y.; Li, X. *Inorg. Chem.* **2009**, *48*, 1105–1113.
(3) Zhang, L.; Wang, W.; Yang, J.; Chen, Z.; Zhang, W.; Zhou, L.; Liu, S. *Appl. Catal., A* **2006**, *308*, 105–110.
(4) Li, L.; Chu, Y.; Liu, Y.; Dong, L. *J. Phys. Chem. C* **2007**, *111*, 2123–2127.
(5) Smith, Y. R.; Kar, A.; Subramanian, V. R. *Ind. Eng. Chem. Res.* **2009**, *48*, 10268–10276.
(6) Jing, L.; Wang, D.; Wang, B.; Li, S.; Xin, B.; Fu, H.; Sun, J. *J. Mol. Catal., A* **2006**, *244*, 193–200.
(7) Stroyuk, A. L.; Shvalagin, V. V.; Kuchmii, S. Y. *J. Photochem. Photobiol., A* **2005**, *173*, 185–194.
(8) Yu, J.; Zhang, L.; Cheng, B.; Su, Y. *J. Phys. Chem. C* **2007**, *111*, 10582–10589.
(9) Yu, J.; Liu, S.; Yu, H. *J. Catal.* **2007**, *249*, 59–66.
(10) Yeber, M. C.; Rodrlguez, J.; Freer, J.; Durán, N.; Mansilla, H. D. *Chemosphere* **2000**, *41*, 1193–1197.
(11) Khodja, A.; Sehili, T.; Pilichowski, J.; Boule, P. *J. Photochem. Photobiol., A* **2001**, *141*, 231–239.
(12) Ye, C.; Bando, Y.; Shen, G.; Golberg, D. *J. Phys. Chem. B* **2006**, *110*, 15146–15151.
(13) Cao, B.; Cai, W. *J. Phys. Chem. C* **2008**, *112*, 680–685.
(14) Zhang, Z.; Shao, C; Li, X.; Zhang, L.; Xue, H.; Wang, C.; Liu, Y. *J. Phys. Chem. C* **2010**, *114*, 7920–7925.

(15) Zhang, Z.; Shao, C; Li, X.; Wang, C.; Zhang, M.; Liu, Y. *ACS Appl. Mater. Interfaces* **2010**, *2*, 2915–2923.
(16) Wang, C.; Zhao, J.; Wang, X.; Mai, B.; Sheng, G.; Peng, P.; Fu, J. *Appl. Catal., B* **2002**, *39*, 269–279.
(17) Song, K.; Park, M.; Kwon, Y.; Lee, H.; Chung, W.; Lee, W. *Chem. Mater.* **2001**, *13*, 2349–2355.
(18) Ostermann, R.; Li, D.; Yin, Y.; McCann, J.; Xia, Y. *Nano Lett.* **2006**, *6*, 1297–1302.
(19) Fu, H.; Xu, T.; Zhu, S.; Zhu, Y. *Environ. Sci. Technol.* **2008**, *42*, 8064–8069.
(20) Zhang, L.; Austin, D.; Merkulov, V.; Meleshko, A.; Klein, K.; Guillorn, M.; Lowndes, D.; Simpson, M. *Appl. Phys. Lett.* **2004**, *84*, 3972–3974.
(21) Unalan, H.; Wei, D.; Suzuki, K.; Dalal, S.; Hiralal, P.; Matsumoto, H.; Imaizumi, S.; Minagawa, M.; Tanioka, A.; Flewitt, A.; Milne, W.; Amaratunga1, G. *Appl. Phys. Lett.* **2008**, *93*, 133116–133118.
(22) Liu, J.; Li, J.; Sedhain, A.; Lin, J.; Jiang, H. *J. Phys. Chem. C* **2008**, *112*, 17127–17132.
(23) Zhang, G.; Sun, S.; Yang, D.; Dodelet, J.; Sacher, E. *Carbon* **2008**, *46*, 196–205.
(24) Chen, L.; Tsai, F.; Fang, S.; Ho, Y. *Electrochim. Acta* **2009**, *54*, 1304–1311.
(25) Ahimou, F.; Boonaert, C.; Adriaensen, Y.; Jacques, P.; Thonart, P.; Paquot, M.; Rouxhet, P. *J. Colloid Interface Sci.* **2007**, *309*, 49–55.
(26) Yu, J.; Yu, X . *Environ. Sci. Technol.* **2008**, *42*, 4902–4907.
(27) Ottaviano, L.; Kwoka, M.; Bisti, F.; Parisse, P.; Grossi, V.; Santucci, S.; Szuber, J. *Thin Solid Films* **2009**, *517*, 6161–6169.
(28) Ros, T.; Van Dillen, A.; Geus, J.; Koningsberger, D. *ChemPhysChem* **2002**, *3*, 209–214.
(29) Mawhinney, D.; Naumenko, V.; Kuznetsova, A.; Yates, J.; Liu, J.; Smalley, R. *J. Am. Chem. Soc.* **2000**, *122*, 2383–2384.
(30) Qin, Y.; Yang, H.; Zhang, X.; Li, P.; Zhou, X.; Niu, Li.; Yuan, W. *Carbon* **2010**, *48*, 3323–3329.
(31) Xiong, H.; Wang, Z.; Xia, Y. *Adv. Mater.* **2006**, *18*, 748–751.
(32) Tang, X.; Choo, E.; Li, L.; Ding, J.; Xue, J. *Langmuir* **2009**, *25*, 5271–5275.
(33) Turchi, C.; Ollis, D. *J. Catal.* **1990**, *122*, 178–192.
(34) Lee, M.; Park, S.; Lee, G.; Ju, C.; Hong, S. *Catal. Today* **2005**, *101*, 283–290.
(35) Woan, K.; Pyrgiotakis, G.; Sigmund, W. *Adv. Mater.* **2009**, *21*, 2233–2239.
(36) Aarthi, T.; Madras, G. *Ind. Eng. Chem. Res.* **2007**, *46*, 7–14.
(37) Rajeshwar, K.; Osugi, M.; Chanmanee, W.; Chenthamarakshan, C.; Zanoni, M.; Kajitvichyanukul, P.; Krishnan, A. R. *J. Photochem. Photobiol., C* **2008**, *9*, 171–192.